

# Large Scale Silicon Photonic MEMS Switch

*Sangyoon Han*

Electrical Engineering and Computer Sciences  
University of California at Berkeley

Technical Report No. UCB/EECS-2015-40

<http://www.eecs.berkeley.edu/Pubs/TechRpts/2015/EECS-2015-40.html>

May 1, 2015



Copyright © 2015, by the author(s).  
All rights reserved.

Permission to make digital or hard copies of all or part of this work for personal or classroom use is granted without fee provided that copies are not made or distributed for profit or commercial advantage and that copies bear this notice and the full citation on the first page. To copy otherwise, to republish, to post on servers or to redistribute to lists, requires prior specific permission.

#### Acknowledgement

This work was supported in part by the National Science Foundation Center for Integrated Access Network (CIAN) under grant #EEC-0812072, National Science Foundation Center for Energy Efficient Electronics Science (E3S) under NSF Award 0939514, and Defense Advanced Research Project Agency (DARPA) Electronic-Photonic Heterogeneous Integration (E-PHI) program.

---

# Large Scale Silicon Photonic MEMS Switch

by Sangyoon Han

---

## Research Project

Submitted to the Department of Electrical Engineering and Computer Sciences,  
University of California at Berkeley, in partial satisfaction of the requirements for the  
degree of **Master of Science, Plan II**.

Approval for the Report and Comprehensive Examination:

### Committee:

---

Professor Ming C. Wu  
Research Advisor

---

(Date)

\* \* \* \* \*

---

Professor Liwei Lin  
Second Reader

---

(Date)

## **ABSTRACT**

Fast optical circuit switches with large port count will allow flexible bandwidth allocation in datacenter networks by augmenting electrical packet switching. Here we report microsecond speed optical circuit switch with 50x50 port counts implemented on silicon photonics platform using MEMS actuated directional couplers. The switch has fast switching speed (2.5  $\mu$ s response time), high on-off extinction ratio (25 dB), small footprint (9x9 mm<sup>2</sup>), and simple fabrication process (3 lithography steps). We believe that our switch port-count can be scaled up to 100 x 100 and beyond.

## 1. INTRODUCTION

Due to the increase of data traffic in datacenter, bandwidth management in the network became a serious issue for enhancing the performance of the datacenter. One promising way to manage the bandwidth in the datacenters is using optical circuit switches to allocate bandwidth between servers [1,2]. By connecting the servers in the datacenters using optical networks, and reconfiguring the connections between the servers by optical circuit switches, one can efficiently manage dynamically varying traffics between servers. 3D MEMS switched has been used for this application, but due to its slow switching time, which is on the order of 1-10ms, the advantage of using it was limited. Silicon photonic switches, of which switching time is on the order of microsecond or less, are a good candidate for the application. Silicon photonics platform provides dense integration of components and seamless interface to CMOS drivers [3]. However, the demonstrations were limited up to 8x8 port count due to its architecture (cascaded 2 x 2) which incurs a high optical insertion loss.

In this paper, we report on a highly scalable optical switch architecture built on silicon photonic platform with MEMS (Microelectromechanical systems) technology. We proved the scalability of the switch by demonstrating 50x50 switch network. Small mass of silicon photonic components allows fast actuation of MEMS, which resulted in fast response of the switch. MEMS actuation also allows high extinction ratio of the switch and low leakage optical loss by changing the light path geometrically rather than refractive index tuning.

## 2. SWITCH DESIGN

### A. Switch Architecture

Figure 1a illustrates our switch architecture. We used silicon waveguides to form optical crossbar network. Light is coupled from fibers to grating couplers, which are located at the end of the switch network. A MEMS actuator with movable directional couplers is located at each mesh of the crossbar network and forms one unit cell, and the actuators can be actuated independently to control the light path.

Each unit cell can have two states; Through-state and Drop-state. When the cell is in Through-state, the MEMS actuator is bent out of plane, and the light comes into in port of the cell simply follows the waveguide and goes to through port. On the other hand, when the cell is in Drop-state, the MEMS actuator with waveguide attached comes down and forms two pairs of directional couplers, and it allows the light to couple between the waveguides and goes to drop port. By selecting the state of the each unit cell, we can route light from any input grating couplers to any output grating couplers simultaneously. For  $N \times N$  switch this architecture has  $N^2$  of switch unit cells, which can be controlled individually. The advantage of this architecture is that for any given light path, the light goes through switching action only once no matter of the port count of the switch network, and rest of the time it stays in passive waveguides. Since the switching action produces more power leakage and insertion loss than guiding through passive

waveguides, our switch architecture has advantage of low insertion loss when the size of the switch scales.

Our optical switch architecture had path dependent insertion loss variation, which is inherent in optical crossbar network. The optical insertion loss is coming from the passive waveguides and the waveguide crossings, which provide connection between the unit cells. Ideally, the insertion loss from the waveguides should be negligible compared to the insertion loss from the waveguide crossings. Most of the waveguide loss is coming from the sidewall roughness induced scattering, which is fabrication process dependent. Practically, the insertion loss from waveguides can be reduced by improving etch profile of the fabrication process [4] and further post processing method [5] which reduce sidewall roughness of the waveguide.

However, the waveguide crossing loss is mostly coming from optical scattering due to the guiding profile change at the crossing point. For the longest optical path for  $N \times N$  crossbar switch, there are  $2N$  of waveguide crossings, which light needs to go through, so the longest path insertion loss of the switch linearly scales with the loss of a waveguide crossing. Thus, we need a very careful design of waveguide crossing to reduce the insertion loss of our switch architecture.

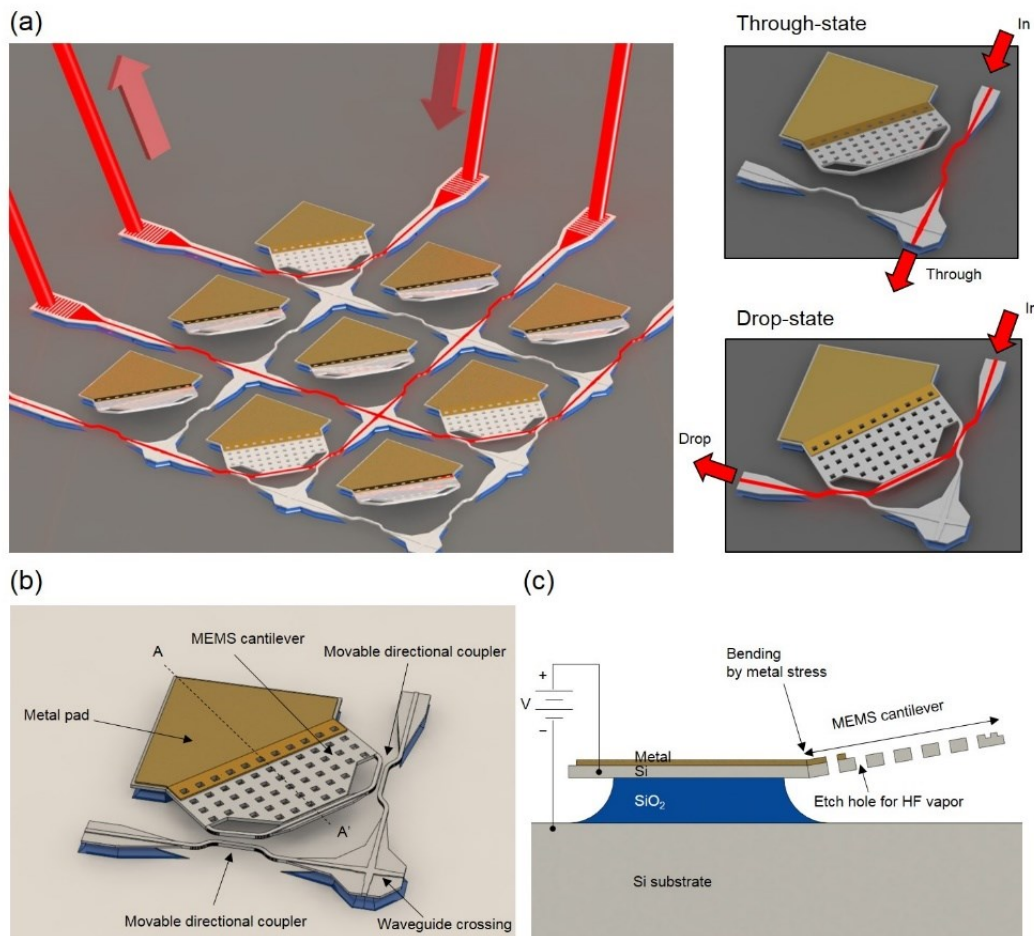


Figure 1. (a) Schematic of the switch architecture. (b) Schematic of the switch unit cell. (c) Cross section view of the switch unit cell.

## B. Switch Unit-cell

Figure 1b describes the unit cell structure of our switch. It consists of one MEMS cantilever actuator with metal probing pad, two pairs of movable directional couplers, one waveguide crossing, ridge waveguides, and waveguide tapers. One pair of directional coupler consists of two waveguides with same width and length. One waveguide of the pair is connected to a ridge waveguide and a waveguide crossing which are anchored on silicon dioxide layer. The other waveguide of the pair is connected to the MEMS cantilever actuator and moves with the actuator. MEMS cantilever actuator can be moved vertically by applying the voltage between the silicon substrate and the actuator through the metal pad. By changing the vertical location of the movable waveguide using the MEMS actuator, we can control the coupling between the two waveguides. When the actuator comes down and movable waveguide is in the same plane as the fixed waveguide, there is strong coupling between the two waveguides and they form a pair of directional coupler. In this configuration light coming from one of the waveguide couples into the other waveguide. By appropriately choosing the length and the width of the waveguides, we can fully transfer the light from one waveguide to the other.

## C. Low Loss Waveguide Crossing

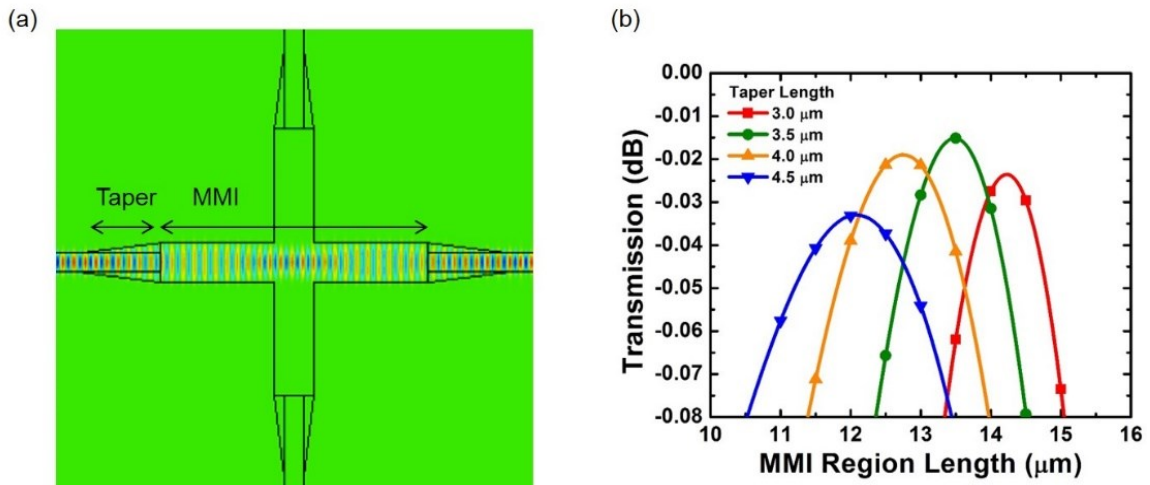


Figure 2. (a) Optical mode profile of the time domain simulation of the waveguide crossing with the optimal dimension. (b) Transmission loss of the waveguide crossing with various dimensions.

The major loss mechanism of the waveguide crossing is the optical scattering at the crossing point. The lateral guiding of the optical mode abruptly changes at the point where the two orthogonal waveguides meet. Our strategy is to reduce the interaction between optical mode and the guiding at the crossing point by focusing the optical mode at the crossing point. To focus the mode, we utilized Multi-Mode Interference (MMI) pattern (Fig. 2a). Interference of the first mode and the 3rd mode (2nd odd mode) of the waveguide can create focusing pattern at the center of the waveguide. In order to excite

the two modes, we gradually tapered the waveguide width from 500 nm to 2  $\mu\text{m}$ . By doing the parameter sweep of the taper length and the MMI length (Fig. 2b), we could find an optimal point, which has the lowest insertion loss. The mode profile of a time domain simulation is shown in Fig 2a, and the parameter sweep result is shown in Fig 2b. The optimal design was found to be with 3.5  $\mu\text{m}$  taper length and 13.5  $\mu\text{m}$  MMI length, and the insertion loss at this dimension was 0.015 dB.

#### D. Movable directional coupler

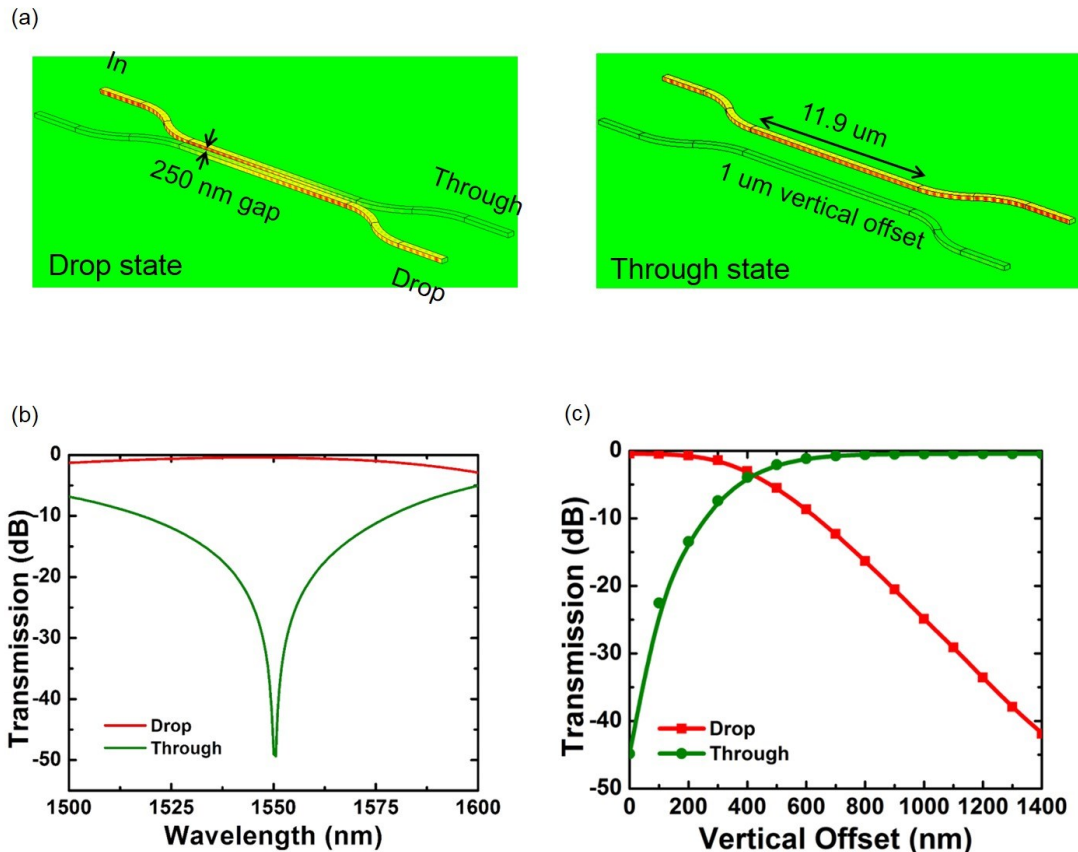


Figure 3. (a) Optical mode profile of directional coupler at Drop-state (left) and Through-state (right). (b) Spectral response of a Movable directional coupler. (c) Transmission characteristics of a Movable directional coupler with different vertical offsets

Figure 3a shows the mode profile of a time domain simulation of a movable directional coupler. A movable directional coupler consists of two identical waveguides in parallel. The width and the thickness of the waveguides are 350 nm and 220 nm respectively. The length of the waveguides is 11.9  $\mu\text{m}$ . Movable directional coupler has two states; “through-state” and “drop-state”. At drop-state, the two waveguides are placed at the same plane with 250 nm gap. In this configuration, the two waveguides are coupled and light from one waveguide completely transfers to the other waveguide. On the other hand, at through-state, two waveguides are vertically away from each other by 1  $\mu\text{m}$ . In this configuration, the two waveguides no longer coupled and the light simply follows the

waveguide, which the light is originally injected in. Figure 3b shows the spectral response of the movable directional coupler in drop-state. The extinction ratio between the drop port and the through port is 50 dB at 1550 nm wavelength.

Figure 3c shows the simulated transmission characteristics of the movable directional coupler with different vertical offsets. At 0  $\mu\text{m}$  vertical offset, when the two waveguides are in the same plane, optical power transfers to the drop port with negligible loss and only -45 dB (relative to the input power) of optical power goes to the through port. On the other hand, at 1  $\mu\text{m}$  vertical offset most of the optical power goes to through port and there are only -25 dB (relative to the input power) of optical power goes to the drop port.

### E. MEMS actuator design

Figure 1c shows the cross section of the MEMS actuator, which controls the vertical offset of the movable directional coupler. The actuator moves up and down by the electrostatic force between the substrate and the cantilever. The voltage applied between the cantilever and the silicon substrate controls the amount of the electrostatic force. The fixed side of the cantilever is extended and anchored on  $\text{SiO}_2$  layer. There is a metal coating on top of the extended part of the cantilever, and the stress in the metal coating [6] bends the cantilever upward by 1  $\mu\text{m}$  when there is no voltage applied. There are etch holes on the cantilever for the HF vapor gas to flow, which etches  $\text{SiO}_2$  layer to release the cantilever in the air. We used a capacitive cantilever beam model to design the MEMS actuator. The thickness of the beam was set at 220 nm, which is the thickness of silicon layer of SOI (Silicon-On-Insulator) wafer we used for fabricating our switch. The gap between the cantilever and the substrate was set as 3  $\mu\text{m}$ , which is the thickness of the buried oxide layer of the SOI wafer. The length of the cantilever was chosen to be 40  $\mu\text{m}$  to have fast actuation speed as well as low voltage operation. The resonant frequency [7] and the pull-in voltage [8] of the cantilever were calculated with the following equations and values:

$$f_{res} = \frac{3.52}{2\pi} \sqrt{\frac{Et^2}{12\rho l^4}} \quad (1)$$

$$V_{pull-in} = \sqrt{\frac{3Et^3 z_0^3}{10\epsilon_0 l^4}} \quad (2)$$

,where  $E = 150$  GPa (Young's modulus of Si),  $t = 220$  nm (thickness of the cantilever),  $\rho = 2.32$   $\text{g}\cdot\text{cm}^{-3}$  (density of silicon),  $l = 40$   $\mu\text{m}$  (length of the cantilever),  $z_0 = 3$   $\mu\text{m}$  (gap between the cantilever and the substrate).

The resonant frequency and the pull-in voltage was calculated as 179 kHz and 24 V respectively.

### 3. EXPERIMENTS

#### A. Fabrication

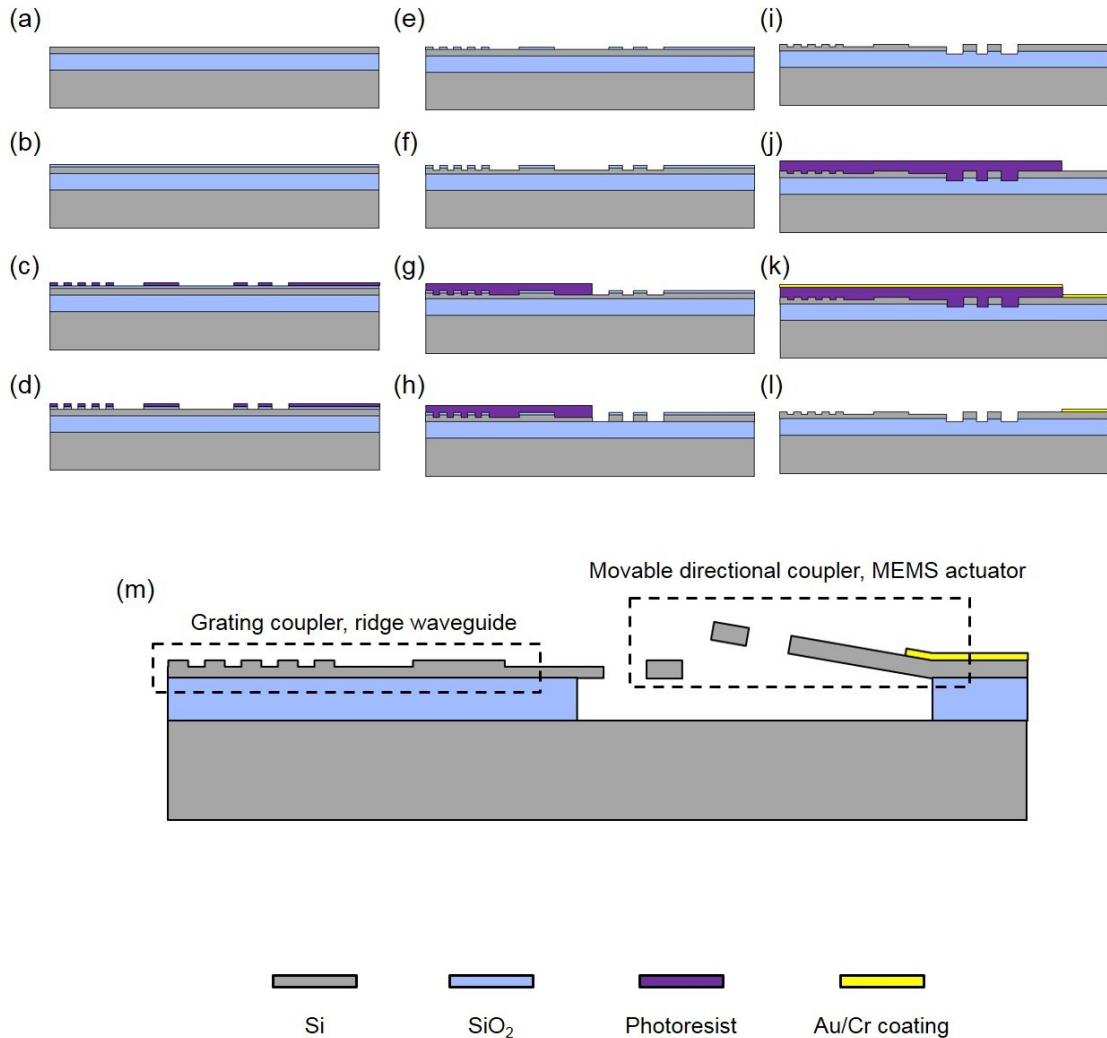


Figure 4. (a) A fresh SOI wafer with 220 nm silicon device layer and 3  $\mu\text{m}$  buried oxide layer. (b) 100 nm low-temperature oxide (LTO) deposited on top of the wafer as etching hardmask layer. (c) Photoresist got patterned by the 1st lithography step. (d) LTO layer got etched. (e) Photoresist got removed. (f) The device layer got etched by 70 nm deep. (g) Photoresist got patterned by the 2nd lithography step. (h) The device layer got etched all the way down to the buried oxide layer. (i) Photoresist got removed. (j) Photoresist got patterned by the 3rd lithography step. (k) Metal (Cr/Au) got evaporated on the wafer. (l) Metal lift-off. (m) Chip got release by HF vapor etching.

The switch chip was fabricated with standard silicon photonic process and HF vapor release process in UC Berkeley Marvell Nanofabrication Laboratory. Figure 4 describes the flow of the fabrication process. It started with SOI (Silicon-On-Insulator) wafer with 220 nm thick device layer and 3  $\mu\text{m}$  buried oxide layer. We first deposited 100 nm thick  $\text{SiO}_2$  on to the wafer as a hardmask for the first etch step. Photoresist was coated on top

of the hardmask and patterned with a deep UV stepper, and then the hardmask was etched all the way down to the device layer using an ICP (Inductively Coupled Plasma) etcher. Photoresist was removed after patterning the hardmask, and the device layer was etched 70 nm deep with a TCP (Transformer Coupled Plasma) etcher. While keeping the remaining hardmask, second lithography was done with the similar condition as the first lithography step, and then the device layer was etched all the way down to the buried oxide layer using a TCP etcher. The last lithography step, which is for the metal lift-off process was followed after removing the photoresist used for the second lithography step. 5 nm thick chrome and 30 nm thick gold was evaporated on the wafer and we used acetone to lift-off the metal. Finally, HF (hydrofluoric acid) vapor etching was used to undercut the buried oxide under the waveguides and actuators to release them in the air. Figure 5 shows the SEM images of the fabricated switch chip. Unit cell size of the switch is  $160 \times 160 \mu\text{m}^2$ . 2,500 switch cells with MEMS actuated directional couplers were monolithically integrated on  $9 \times 9 \text{ mm}^2$  chip area.

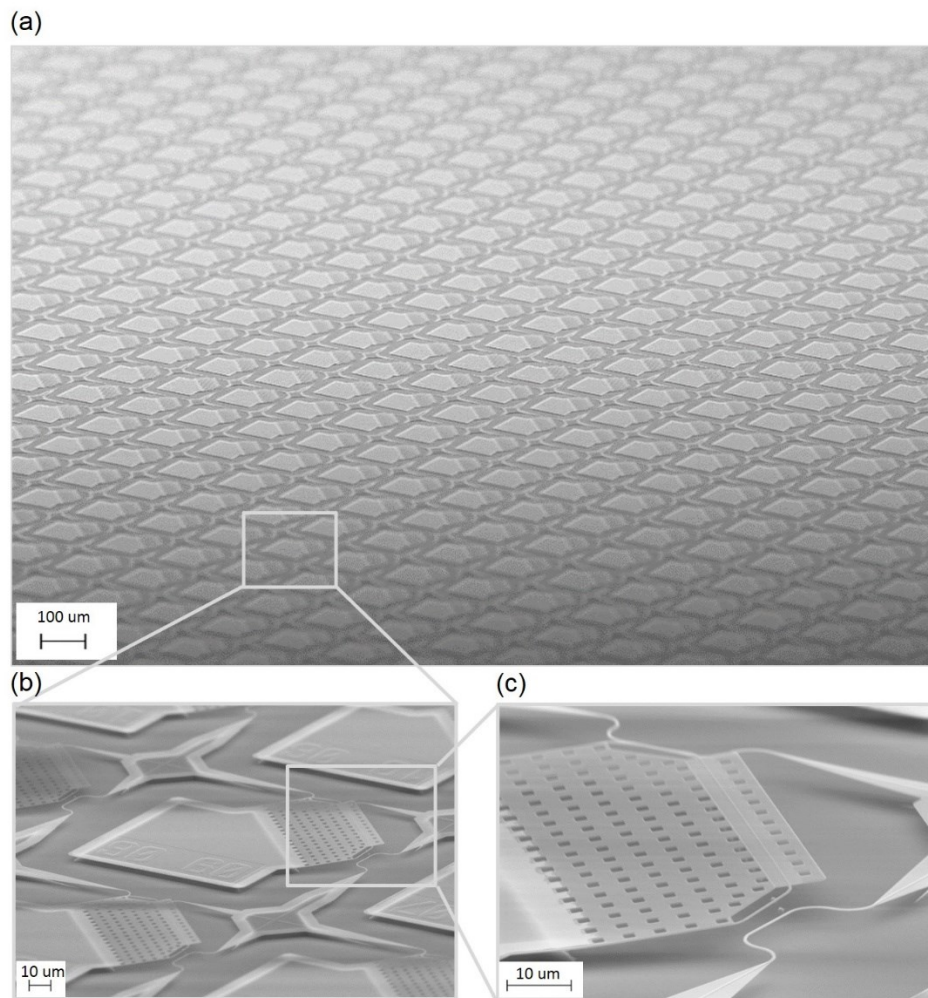


Figure 5. (a) SEM image of 50x50 switch chip array. (b) Zoomed in SEM image of the array. (c) SEM of a switch unit cell.

## B. Measurement method

Figure 6a shows a photograph and a schematic of the switch chip on the measurement setup. The switch chip was mounted on a chip carrier and a set of fiber array was used to couple light into the chip. Tungsten probe tip with 5  $\mu\text{m}$  radius tip was used to electrically probe the switch cells. The fiber array is attached to alignment stage with 6 degree of freedom to allow precise alignment between the fiber array and the switch chip. In order to measure the large switch array using a single fiber array, we put a grating coupler array at one side of the chip and routed waveguides to the subset of the switch array (Fig. 6b). The fibers in the fiber array were terminated with FC/APC connectors. The connectors were connected to a tunable laser source and optical power meters to characterize the properties of the switch.

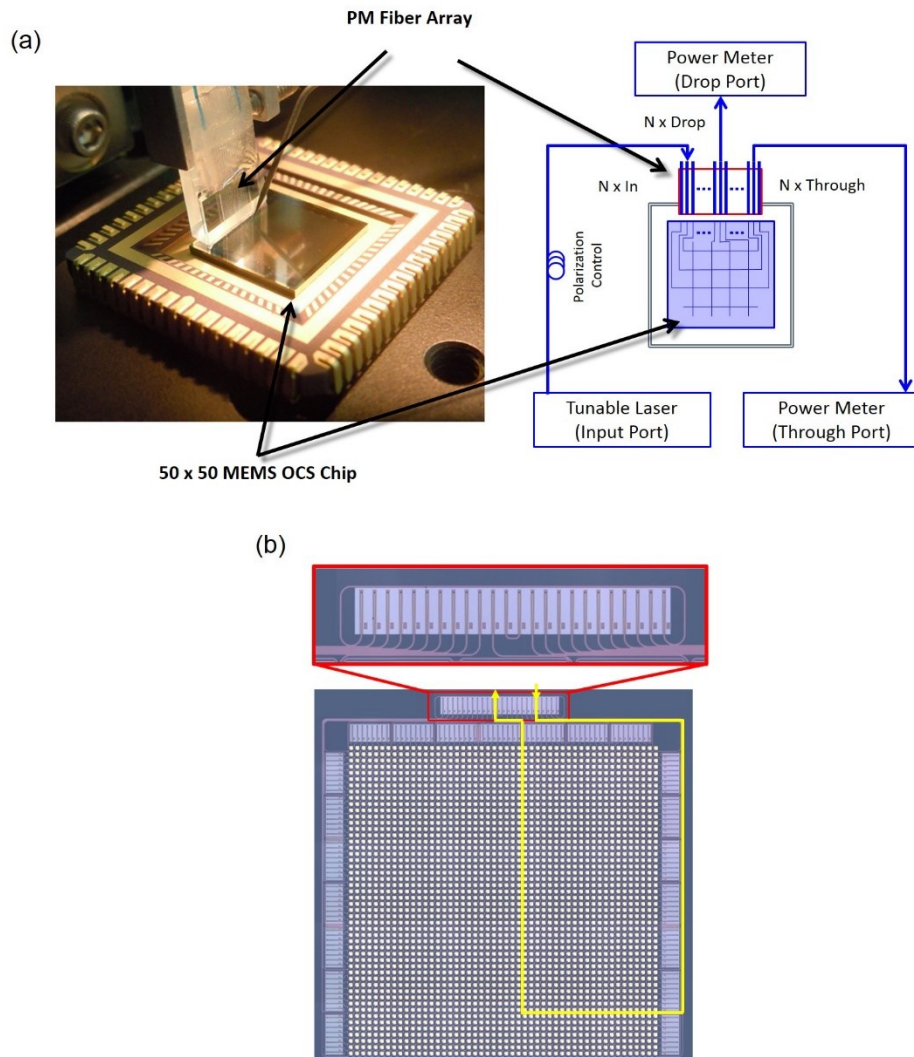


Figure 6. (a) Photograph (left) and schematic (right) of the switch chip mounted on a chip carrier with a fiber array aligned to it. (b) Optical microscope image of the switch chip with an example of a light path (yellow line).

### C. Transmission characteristics of the switch with voltage bias

We measured transmission characteristics of the switch cells with different voltage bias applied. Figure 7 shows measured transfer curve with voltage bias from 0 V to 14.2 V. At 14 V, the switch reached the point where the extinction ratio between the drop port and the through port is the maximum. The on-off extinction ratio for both the drop port and the through port was larger than 25 dB. The graph also shows the fact that the transmitted power to the drop port and the through port rapidly changes between 10 V to 14 V, and it allows to operate the switch with low actuation voltage with DC bias added.

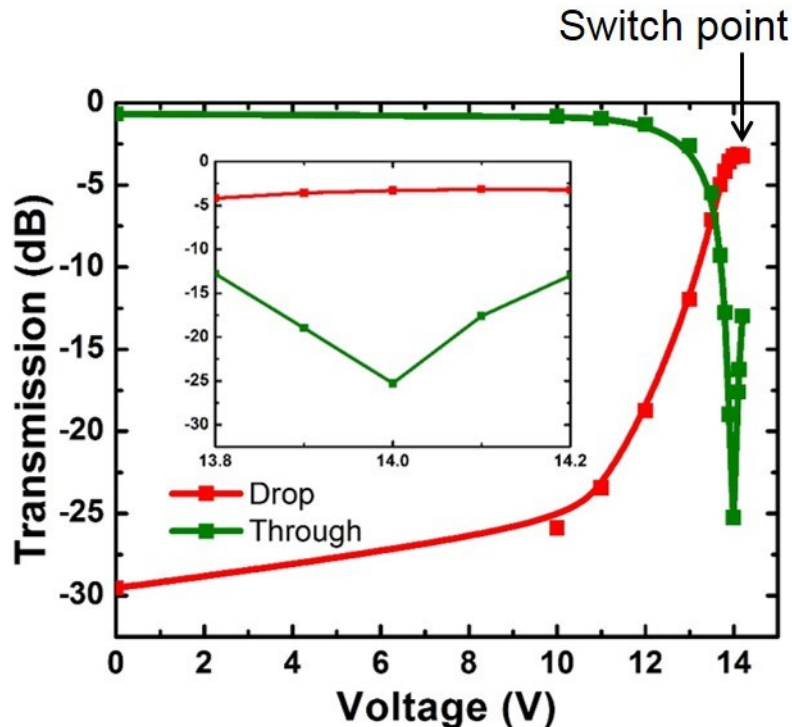


Figure 7. Measured transfer characteristic of the switch with different voltage bias.

### D. Spectral response of the switch

Figure 8 shows the both simulated and measured spectral response of the switch unit cell at the optimal switching point. Since there are two MEMS actuated directional couplers for drop port path, the spectral response of the drop port of the unit cell is multiplication of two MEMS actuated directional coupler. Thus for the simulated value, we assumed two cascaded identical directional couplers for the drop port. The wavelength range we measured was limited by our tunable laser, which had tuning range from 1460 nm to

1580 nm. As shown in the graph, the measured spectral response of the switch unit cell well agrees with the simulated values. The largest extinction ratio between the drop port and the through port was near 1550 nm for both simulated and measured result. The small discrepancy between the measurement result and the simulation result mostly came from the non-ideal width of the waveguides in the directional couplers.

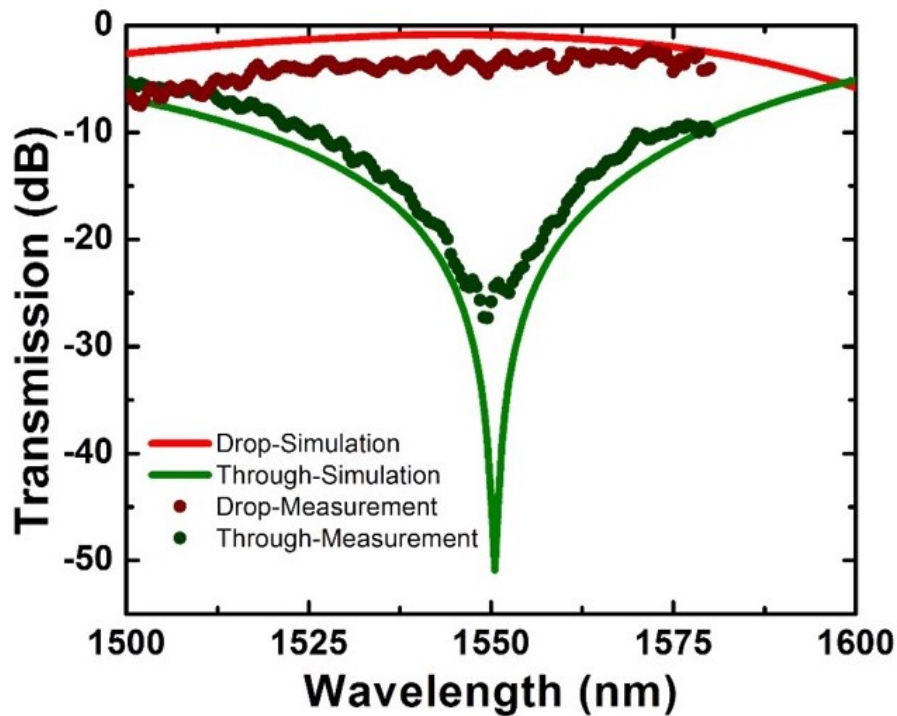


Figure 8. Measured (dots) and simulated (lines) spectral response of the switch unit cell

### E. Switch temporal response

Figure 9a shows the temporal response of the switch respected to the step voltage applied to the switch. The switch reached the 90% of the set power within 2.5  $\mu\text{s}$  for turning on, and reached 10% of the set power within 3.8  $\mu\text{s}$  for tuning off. There were some ripples in the optical power trace due to the vertical ringing of the MEMS actuator. The ringing can be suppressed by using more sophisticated driving voltage shape.

Figure 9b shows the frequency response of the MEMS actuator. We measured the vertical motion of the MEMS actuator in response to the bias voltage with different frequencies by using LDV (Laser Doppler Vibrometer) measurement. The resonance peak of the vibration was near 163 kHz, and it well agrees with the calculated resonant frequency (179 kHz). For the future, switch with faster response time can be made with stiffer MEMS actuator with higher resonant frequency.

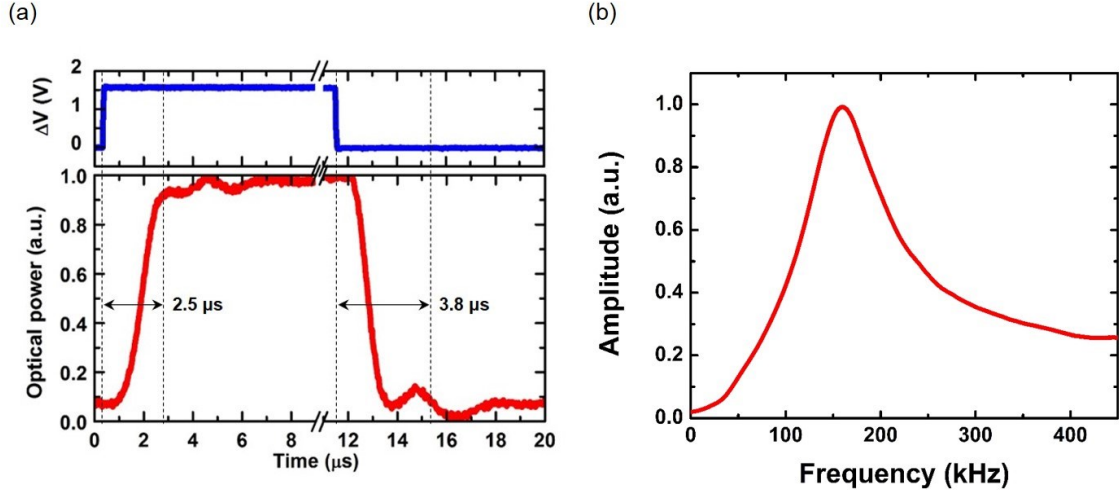


Figure 9. (a) Measured time response of the switch to the step voltages applied. (b) Measured frequency response of the MEMS actuator.

## F. Optical insertion loss of switch

In order to characterize the path dependent loss of our switch, we measured insertion loss of several optical paths with different path length (Fig. 10a). The grating coupler loss was measured on grating coupler test structures and subtracted from the measured values. Due to the fabrication variation on the switch chip, the average waveguide width in the movable directional couplers was defined to be 430 nm. The insertion loss of the longest path, which contains 98 cell in Through-state and one cell in Drop-state, was 27.5 dB. By linear fitting of the measured insertion loss data, we could extract the insertion loss of a through-state cell, which corresponds to the slope of the fitted line. The insertion loss of a through-state cell was 0.253 dB/cell. The Y-intercept of the fitted line was -2.47 dB and it corresponds to drop-state loss of the switch cell. Insertion loss of a drop-state cell can be eliminated with better dimension control of movable directional couplers at the lithography step.

For our switch architecture, there is only one of drop-state cell for any given path, so the drop-state loss does not scale as the switch size increases. However, there are  $2N-2$  of through-state cells for the longest optical path in  $N \times N$  switch. Thus, the through-state cell loss is one of the major issue as the switch size scales. The through-state loss is coming from two sources, loss of waveguide crossings, and propagation loss of the waveguides. In order to characterize the loss of the waveguide crossings, we fabricated waveguide crossing loss test structures, which consist of back-to-back waveguide crossings in series. There were different numbers of the waveguide crossing in the different test structures. The loss of the each test structure was measured and the loss per one waveguide crossing was extracted by linear fitting of the measured loss (Fig. 10b). The loss per waveguide crossing was extracted as 0.038 dB. The propagation loss of the waveguide is mainly coming from the optical scattering loss due to roughness on the sidewall of the

waveguides, and hence it can be reduced by fabricating the switch with more advanced fabrication process which gives smooth etch profile for the waveguide sidewall.

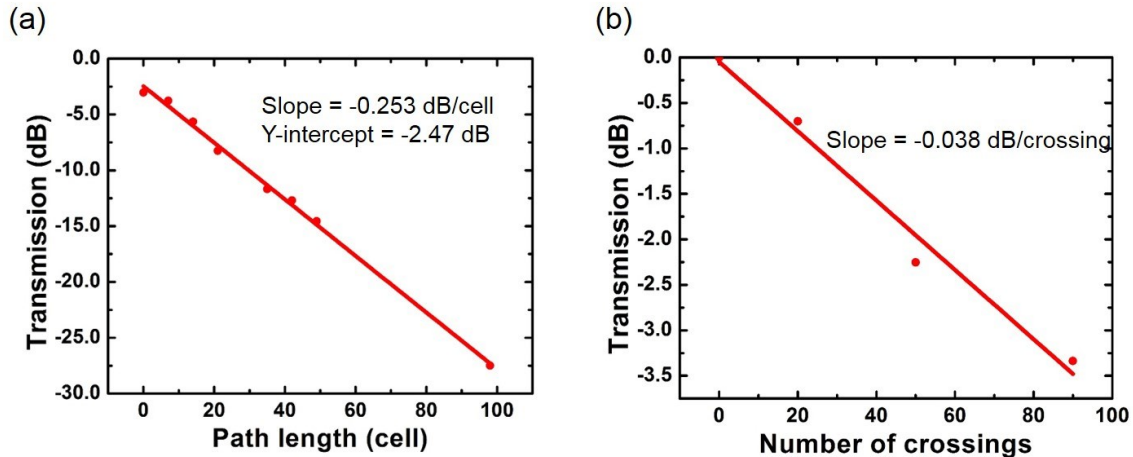


Figure 10. (a) Measured insertion loss of several optical paths with different path length. (b) Measured insertion loss of the waveguide crossing test structures with different numbers in series.

## 4. CONCLUSION

We have reported design, fabrication, and characterization of 50x50 silicon photonics MEMS switch. 2,500 (50x50) switching cells with MEMS actuators were integrated on standard silicon photonics platform with 9x9 mm<sup>2</sup> area. To our knowledge, our switch has the largest port-count among the silicon photonic switches ever reported.

Movable directional couplers integrated on optical crossbar network allowed the high extinction ratio (25 dB) and fast switching speed (2.5  $\mu$ s response time) as well as the large scalability of the switch. Our demonstration showed that the integration of MEMS technology into silicon photonics platform could greatly benefit the integrated optics technology.

## ACKNOWLEDGEMENT

*This work was supported in part by the National Science Foundation Center for Integrated Access Network (CIAN) under grant #EEC-0812072, National Science Foundation Center for Energy Efficient Electronics Science (E3S) under NSF Award 0939514, and Defense Advanced Research Project Agency (DARPA) Electronic-Photonic Heterogeneous Integration (E-PHI) program.*

## REFERENCES

- [1] G. Porter, R. Strong, N. Farrington, A. Forencich, T. Rosing, Y. Fainman, G. Papen, A. Vahdat, and U. C. S. Diego, "Integrating Microsecond Circuit Switching into the Data Center," *ACM SIGCOMM Comput. Commun. Rev.*, vol. 43, no. 4, pp. 447–458, 2013.
- [2] N. Farrington, G. Porter, S. Radhakrishnan, H. H. Bazzaz, V. Subramanya, Y. Fainman, G. Papen, and A. Vahdat, "Helios : A Hybrid Electrical / Optical Switch Architecture for Modular Data Centers," *ACM SIGCOMM Comput. Commun. Rev.*, vol. 40, no. 4, pp. 339–350, 2010.
- [3] B. G. Lee, A. V Rylyakov, W. M. J. Green, S. Assefa, C. W. Baks, R. Rimolodonio, D. M. Kuchta, M. H. Khater, T. Barwicz, C. Reinholm, E. Kiewra, S. M. Shank, C. L. Schow, and Y. A. Vlasov, "Monolithic Silicon Integration of Scaled Photonic Switch Fabrics, CMOS Logic, and Device Driver Circuits," *J. Light Technol.*, vol. 32, no. 4, pp. 743–751, 2014.
- [4] S. K. Selvaraja, W. Bogaerts, and D. Van Thourhout, "Loss reduction in silicon nanophotonic waveguide micro-bends through etch profile improvement," *Opt. Commun.*, vol. 284, no. 8, pp. 2141–2144, Apr. 2011.
- [5] M.-C. M. Lee and M. C. Wu, "Thermal Annealing in Hydrogen for 3-D Profile Transformation on Silicon-on-Insulator and Sidewall Roughness Reduction," *J. Microelectromechanical Syst.*, vol. 15, no. 2, pp. 338–343, Apr. 2006.
- [6] R. T. Wu, Ming C. Chen, "A High-Speed Low-Voltage Stress-Induced Micromachined 2 x 2 Optical Switch," vol. 11, no. 11, pp. 1396–1398, 1999.
- [7] W. C. Young, "Roark's formulas for stress & strain 6th edition." McGraw-Hill, 1989.
- [8] G. J. O. Brien, D. J. Monk, and L. Lin, "MEMS cantilever beam electrostatic pull-in model," *SPIE*, vol. 4593, pp. 31–41, 2001.